BAMS Supplement

Extreme Precipitation on Consecutive Days Occurs More Often in a Warming Climate

Haibo Du, Markus G. Donat, Shengwei Zong, Lisa V. Alexander, Rodrigo Manzanas, Andries Kruger, Gwangyong Choi, Jim Salinger, Hong S. He, Mai-He Li, Fumiaki Fujibe, Banzragch Nandintsetseg, Shafiqur Rehman, Farhat Abbas, Matilde Rusticucci, Arvind Srivastava, Panmao Zhai, Tanya Lippmann, Ibouraïma Yabi, Michael C. Stambaugh, Shengzhong Wang, Altangerel Batbold, Priscilla Teles De Oliveira, Muhammad Adrees, Wei Hou, Claudio Moises Santos E Silva, Paulo Sergio Lucio, and Zhengfang Wu

https://doi.org/10.1175/BAMS-D-21-0140.2
Corresponding author: Dr. Haibo Du, duhb655@nenu.edu.cn; Dr. Markus Donat, markus.donat@bsc.es
Haibo Du and Markus G. Donat contributed equally to this work.
This is a supplement to https://doi.org/10.1175/BAMS-D-21-0140.1

AFFILIATIONS: Du*—Key Laboratory of Geographical Processes and Ecological Security in Changbai Mountains, Ministry of Education, School of Geographical Sciences, and Key Laboratory of Vegetation Ecology, Ministry of Education, Northeast Normal University, Changchun, China; **Donat***—Barcelona Supercomputing Center, and ICREA, Barcelona, Spain; **Zong and Wang**—Key Laboratory of Geographical Processes and Ecological Security in Changbai Mountains, Ministry of Education, School of Geographical Sciences, Northeast Normal University, Changchun, China; **Alexander**—Climate Change Research Centre, and ARC Centre of Excellence for Climate Extremes, University of New South Wales, Sydney, New South Wales, Australia; **Manzanas**—Meteorology Group, Departamento de Matemática Aplicada y Ciencias de la Computación, Universidad de Cantabria, Santander, Spain; **Kruger**—Climate Service Department, South African Weather Service, and Department of Geography, Geoinformatics and Meteorology, Faculty of Natural and Agricultural Sciences, University of Pretoria, Pretoria, South Africa; **Choi**—Geography Education, Jeju National University, Jeju-si, Jeju, South Korea; **Salinger**—School of Geography, Environment and Earth Sciences, Victoria University of Wellington, Wellington, New Zealand; **He**—School of Natural Resource, University of Missouri, Columbia, Missouri, and Key Laboratory of Geographical Processes and Ecological Security in Changbai Mountains, Ministry of Education, School of Geographical Sciences, Northeast Normal University, Changchun, China; **Li**—Key Laboratory of Geographical Processes and Ecological Security in Changbai Mountains, Ministry of Education, School of Geographical Sciences, Northeast Normal University, Changchun, China, and Swiss Federal Research Institute (WSL), Birmensdorf, Switzerland; **Fujibe**—Department of Geography, Tokyo Metropolitan University, Hachioji, Japan; **Nandintsetseg**—Eurasia Institute of Earth Sciences, Istanbul Technical University, Istanbul, Turkey, and Information and Research Institute of Meteorology, Hydrology and Environment, Ulaanbaatar, Mongolia, and Graduate School of Environmental Studies, Nagoya University, Nagoya, Japan; **Rehman**—Interdisciplinary Research Center for Renewable Energy and Power Systems, Research Institute, King Fahd University of Petroleum and Minerals, Dhahran, Saudi Arabia; **Abbas**—School of Climate Change and Adaptation, University of Prince Edward Island, Charlottetown, Prince Edward Island, Canada; **Rusticucci**—Departamento de Ciencias de la Atmósfera y los Océanos, Universidad de Buenos Aires/CONICET, Buenos Aires, Argentina; **Srivastava**—National Climate Centre, India Meteorological Department, Pune, India; **Zhai**—State Key Laboratory of Severe Weather, Chinese Academy of Meteorological Sciences, CMA, Beijing, China; **Lippmann**—Climate Change Research Centre, and ARC Centre of Excellence for Climate Extremes, University of New South Wales, Sydney, New South Wales, Australia, and Department of Earth Sciences, Vrije Universiteit Amsterdam, Amsterdam, Netherlands; **Yabi**—Laboratory "Pierre PAGNEY," Climat, Eau, Ecosystème Développement (LACEEDE), Department of Geography and Planning, University of Abomey-Calavi, Abomey-Calavi, Benin; Stambaugh—School of Natural Resource, University of Missouri, Columbia, Missouri; **Batbold**—Information and Research Institute of Meteorology, Hydrology and Environment, Ulaanbaatar, Mongolia; **Oliveira**—School of Sciences, São Paulo State University (UNESP), Bauru, São Paulo, Brazil; **Adrees**—School of Climate Change and Adaptation, University of Prince Edward Island, Charlottetown, Prince Edward Island, Canada, and Department of Environmental Sciences and Engineering, Government College University Faisalabad, Faisalabad, Pakistan; **Hou**—National Climate Center, China Meteorological Administration, Beijing, China; **Silva and Lucio**—Departament of Atmospheric and Climatic Sciences, Graduate Program in Climatic Sciences, Federal University of Rio Grande do Norte, Natal, Brazil; **Wu**—Key Laboratory of Geographical Processes and Ecological Security in Changbai Mountains, Ministry of Education, School of Geographical Sciences, and Key Laboratory of Vegetation Ecology, Ministry of Education, Northeast Normal University, Changchun, China

Figures A1–A15 were given to quantify our study in more detail.

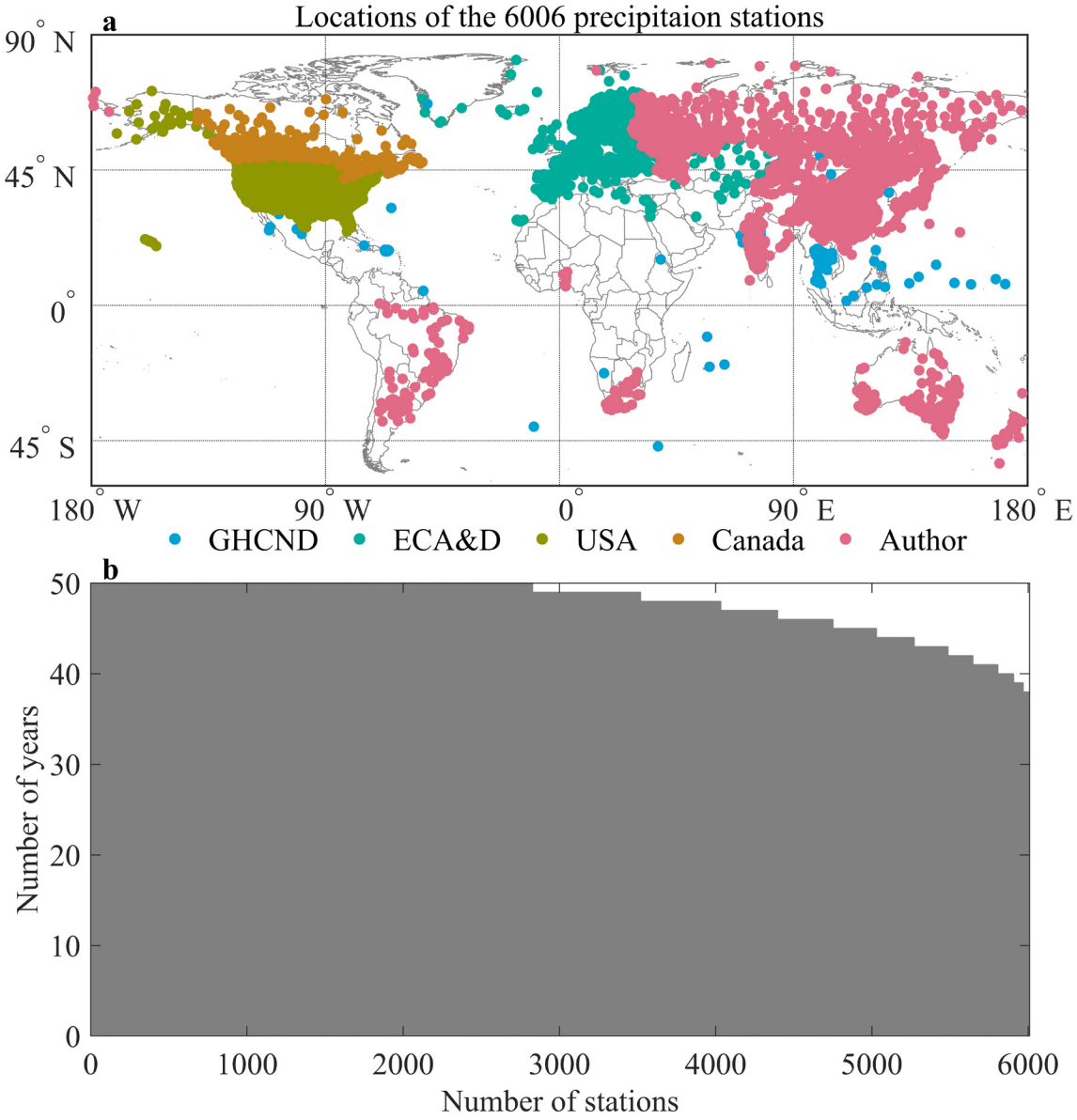

Fig. ES1. Information of the station data. (a) Locations of the 6,006 precipitation stations used for this study. Daily precipitation of these stations in 1961–2010 passed the homogeneity and quality checks. Each color is indicative of a different data source. (b) Number of years of the 6,006 stations used for this study.

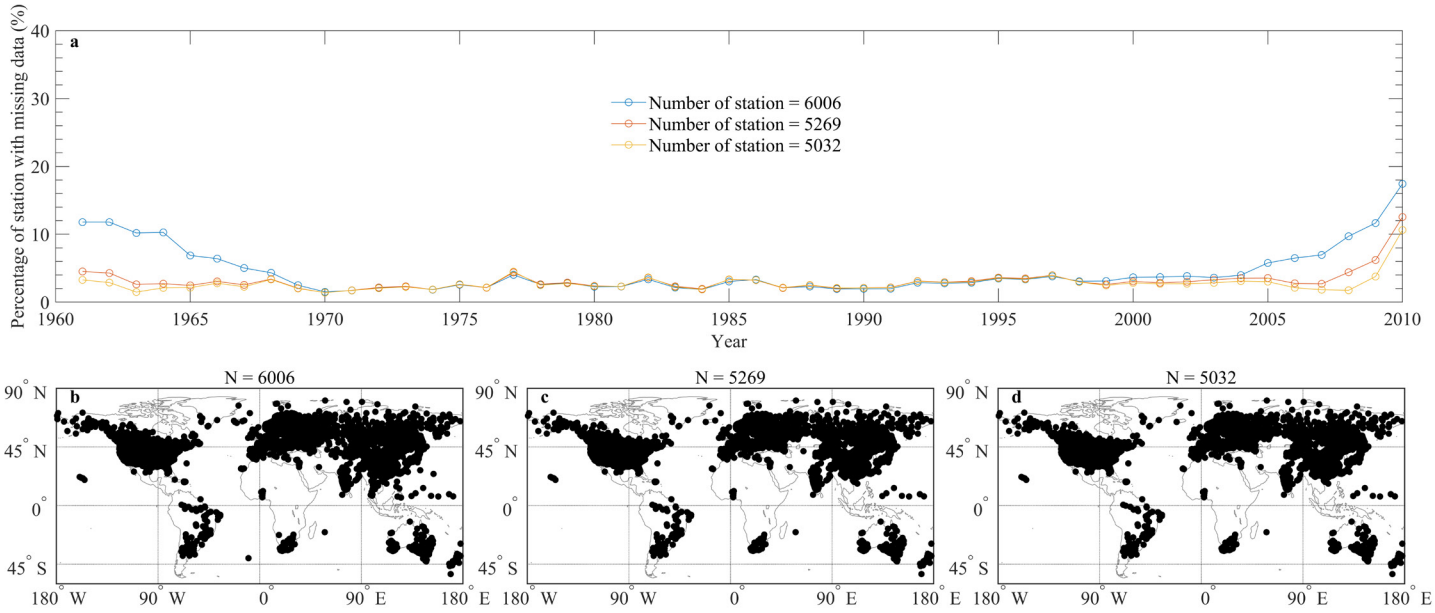

Fig. ES2. Time series of the percentage of missing values and the spatial distribution of three observed datasets. (a) The annual percentage of stations with missing data. Any year with more than 10% of missing values is treated as a "missing year" (see "Materials and methods" section in the main text). Blue represents all stations (6,006) of the original dataset. Orange (yellow) show the remaining 5,269 (5,032) stations after excluding stations from the original dataset if more than 3 years (2 years) have missing data in the beginning or the end 5 years. (b)–(d) The location of the stations for the three datasets.

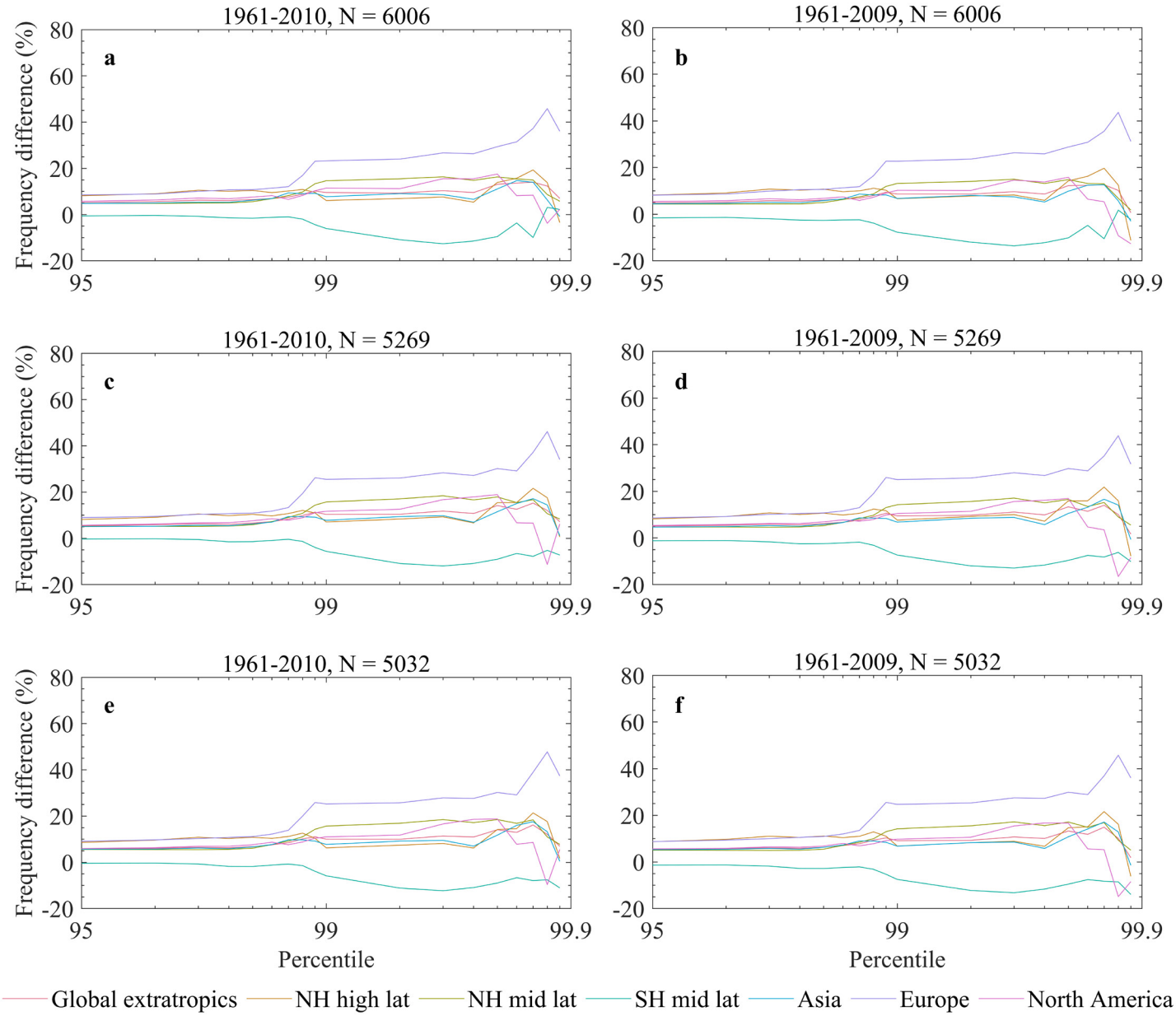

Fig. ES3. The changes (%) in the observed frequency of EPCD between 1961–85 and 1986–2010 (or 1986–2009) using different percentile thresholds for (top to bottom) different datasets (Fig. ES2) and different periods: (left) 1961–2010 and (right) 1961–2009.

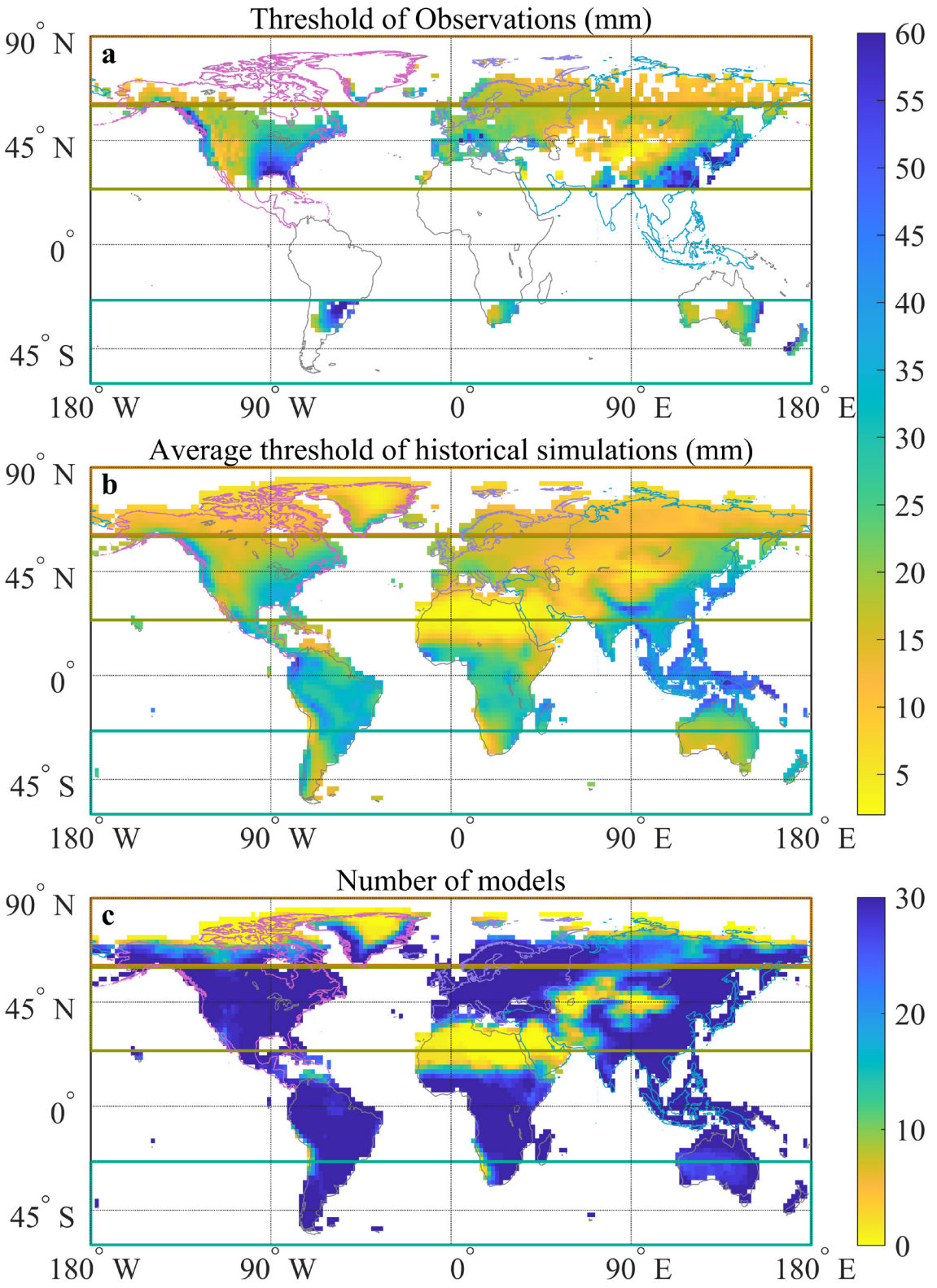

Fig. ES4. The global spatial patterns of the 99th-percentile threshold (mm) of all-day precipitation during 1961–2010 for observations and GCM historical + RCP8.5 scenario simulations. (a) Threshold calculated from the observations. The threshold is first calculated from daily station time series and then interpolated on a regular grid of 2° × 2° horizontal resolution using bilinear interpolation algorithm. (b) Average threshold based on global climate model (GCM) simulations. (c) The number of models with threshold exceeding 10 mm day^{-1} (heavy precipitation) at each grid cell. We merge the historical (1961–2005) and RCP8.5 (2006–10) simulations to have the CMIP5 past data over exactly the same period as observations, i.e., data for 1961–2010 (see "Materials and methods" section in the main text).

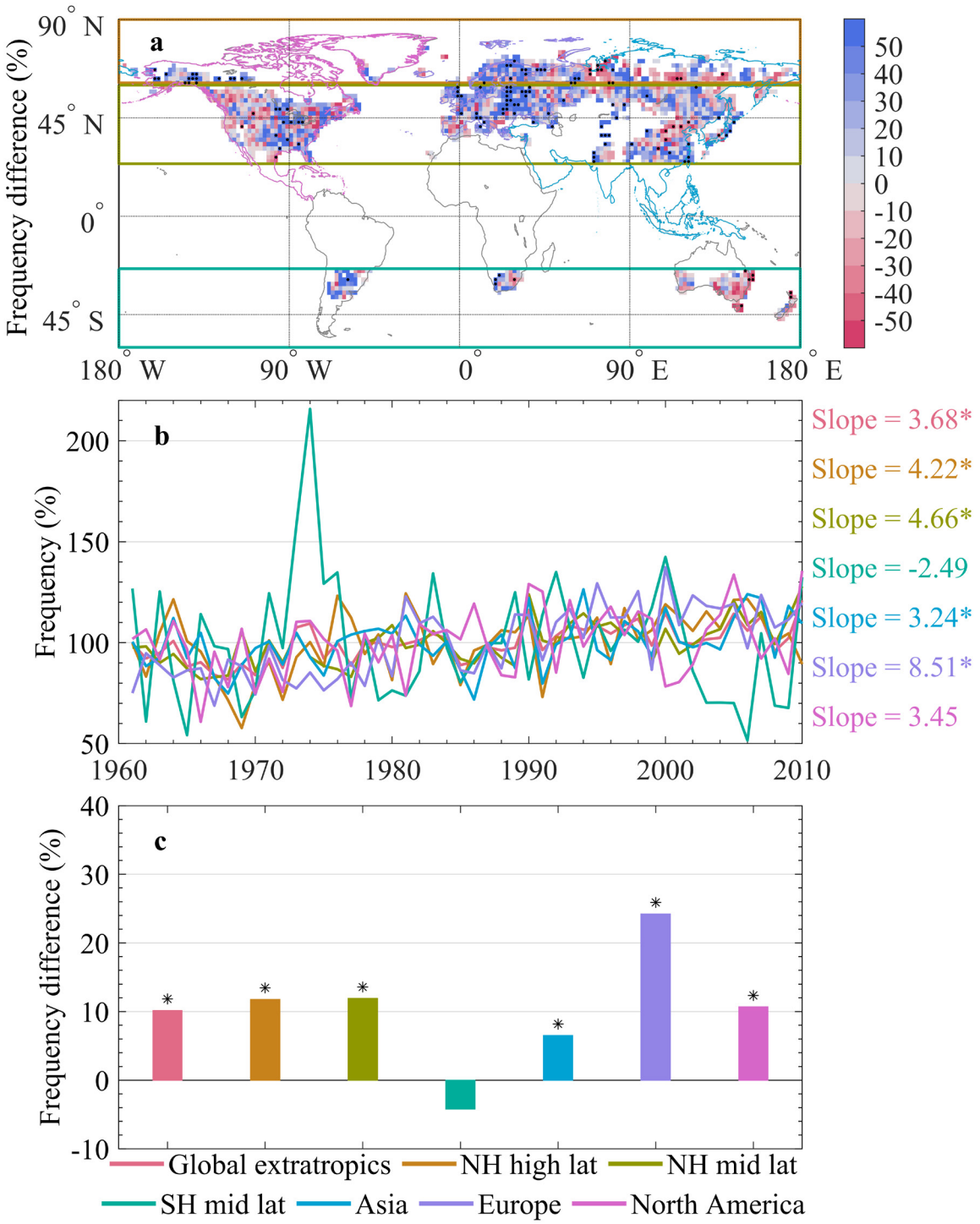

Fig. ES5. Changes in annual frequency of extreme precipitation on consecutive days for observations in 1961–2010. As in Fig. 1, but the grid cells with a threshold smaller than 10 mm are excluded from the analysis (see "Materials and methods" section in the main text).

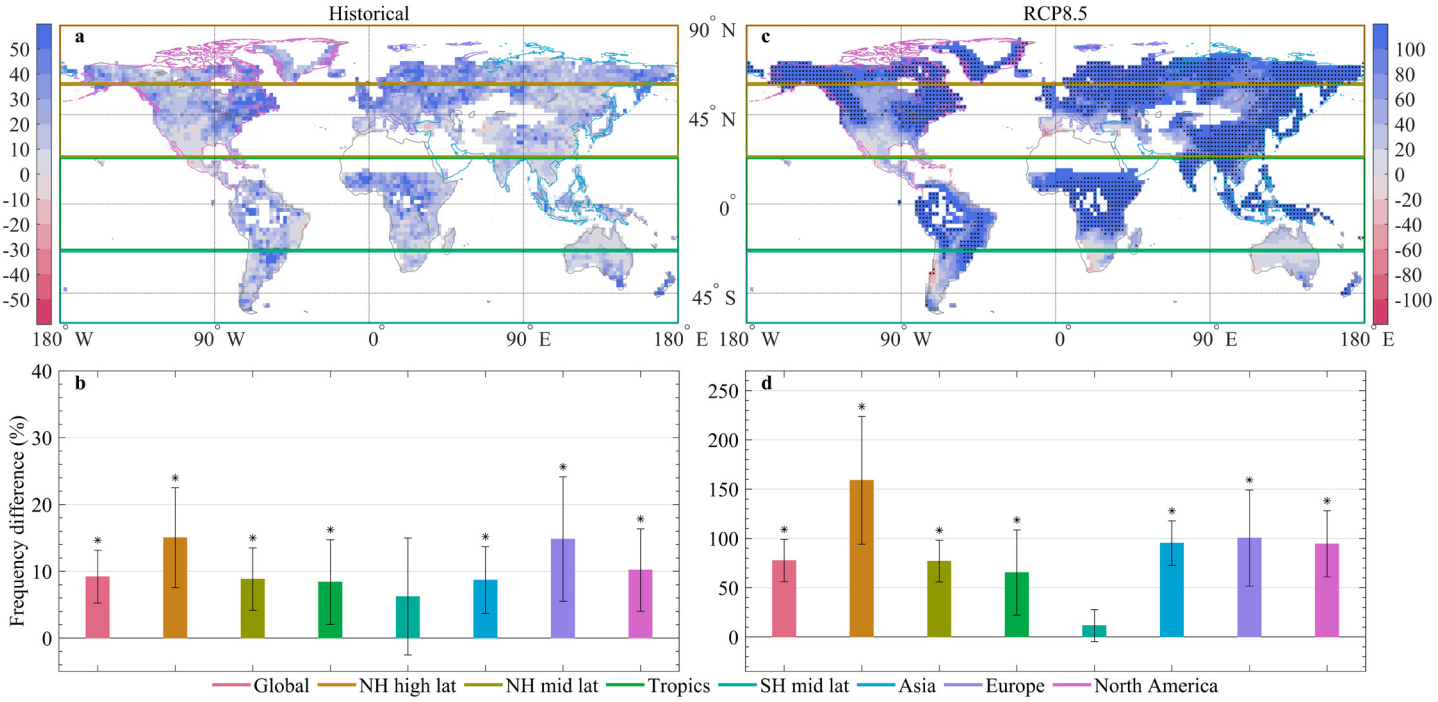

Fig. ES6. Changes in the frequency of extreme precipitation on consecutive days for (left) historical and (right) future simulations. As in Fig. 2, but grid cells with more than 15 models having a threshold smaller than 10 mm are excluded from the regional change analysis and models having these low thresholds are excluded from the local change analysis (see "Materials and methods" section in the main text).

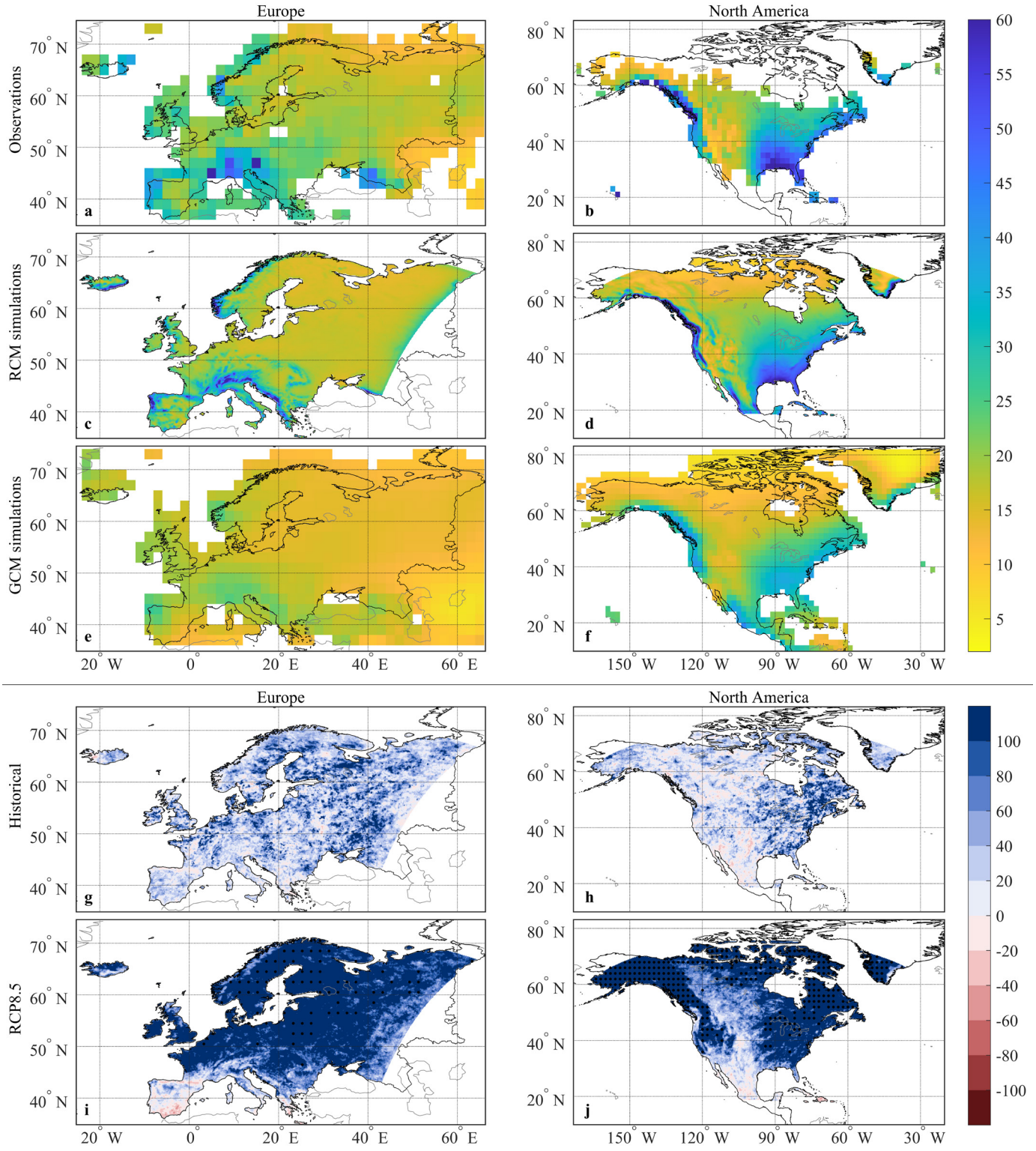

Fig. ES7. The spatial patterns of the 99th-percentile threshold (mm) of all-day precipitation during 1961–2010 and local changes in EPCD frequency for observations and RCM historical + RCP8.5 scenario simulations for (left) Europe and (right) North America. (a),(b) Threshold calculated from the observations. The threshold is first calculated from daily station time series and then interpolated on a regular grid of 2° × 2° horizontal resolution using bilinear interpolation algorithm. (c),(d) Threshold based on regional climate model (RCM) simulations. (e),(f) Threshold based on global climate model (GCM) simulations. (g),(h) Local EPCD frequency changes (%) between 1961–85 and 1986–2010 for RCM historical simulations. (i),(j) Local EPCD frequency changes (%) between 1961–2010 and 2071–2100 for RCM historical + RCP8.5 scenario simulations. We merge the historical (1961–2005) and RCP8.5 (2006–10) simulations to have the CMIP5 past data over exactly the same period as observations, i.e., data for 1961–2010 (see "Materials and methods" section in the main text). The stippling in (e)–(h) indicates a "robust change" across all models (see "Materials and methods" section in the main text).

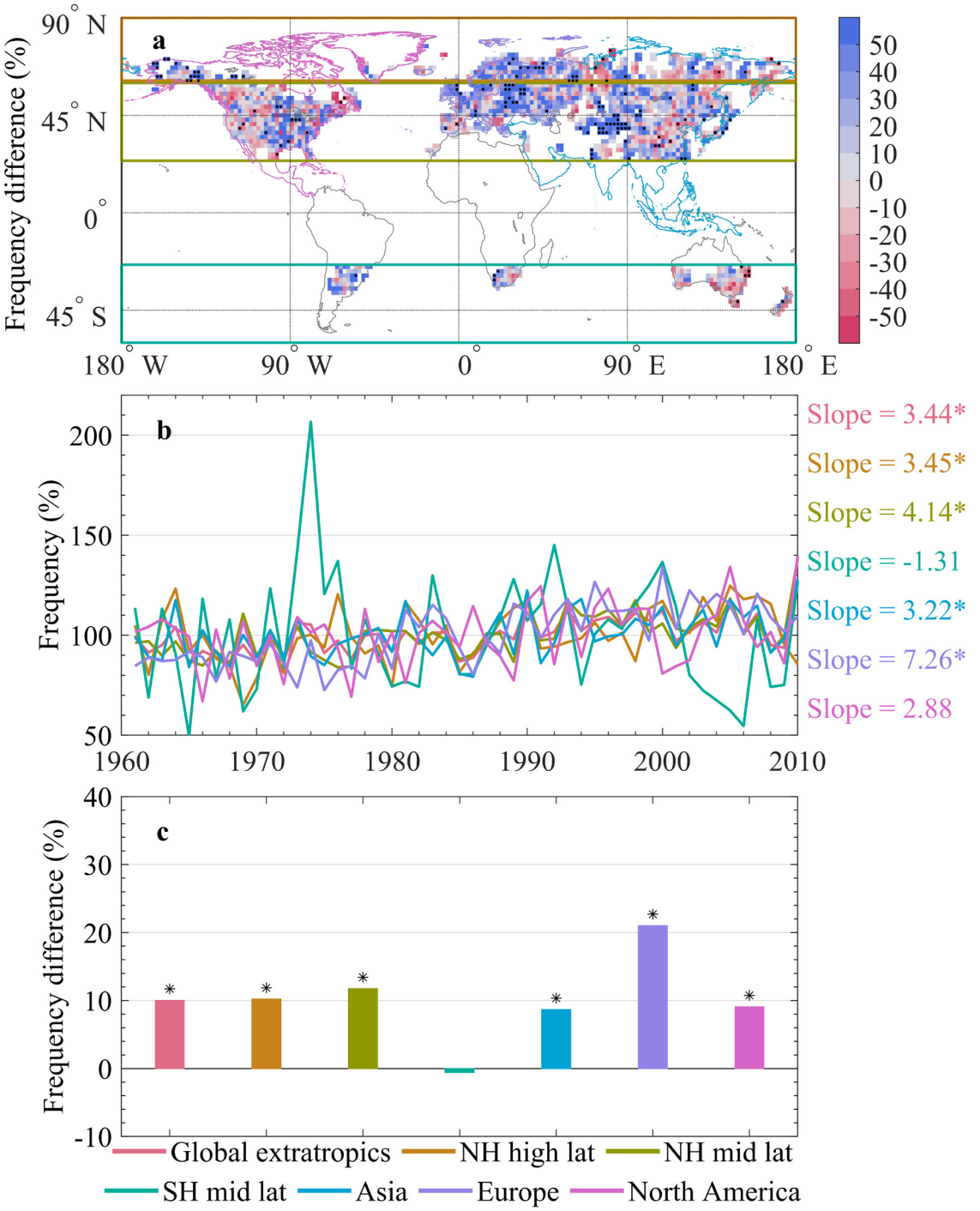

Fig. ES8. Changes in annual frequency of extreme precipitation on consecutive days identified from observations in 1961–2010. These results are based on the alternative definition of EPCD, which can include events where two or more extreme precipitation days are separated by one nonextreme day (see "Materials and methods" section in the main text). (a) Local changes (%) in mean frequency between 1961–85 and 1986–2010. (b) Hemispheric and continental average time series in 1961–2010. The annual frequency is normalized by the mean in 1961–2010. Slope (% decade^{-1}) is the linear trend by the ordinary least squares method. (c) Changes (%) in the regional mean between both periods. The difference is a relative frequency change (see "Materials and methods" section in the main text). The stippling in (a) and the asterisks in (b) and (c) indicate a significant change ($p \leq 0.05$) according to the Wilcoxon rank sum test in (a) and (c) and the Mann–Kendall test in (b). The colored boxes or outlines in (a) define the regions for calculating the regional averages as presented by lines or bars of the corresponding colors in (b) and (c).

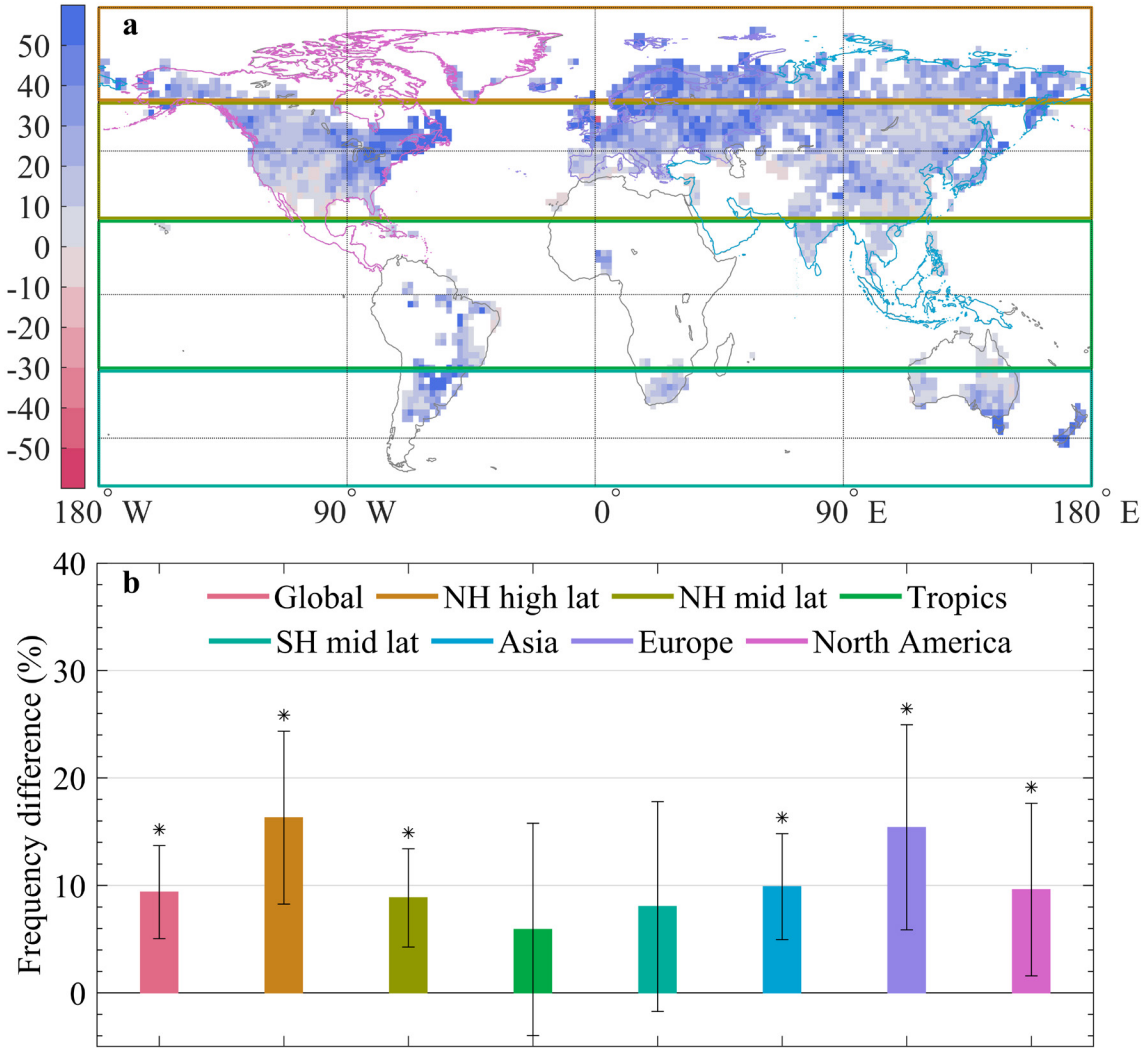

Fig. ES9. The spatial patterns of the frequency anomaly of extreme precipitation on consecutive days (which is normalized by the mean in 1961–2010) during 1973–75 for SH midlatitudes.

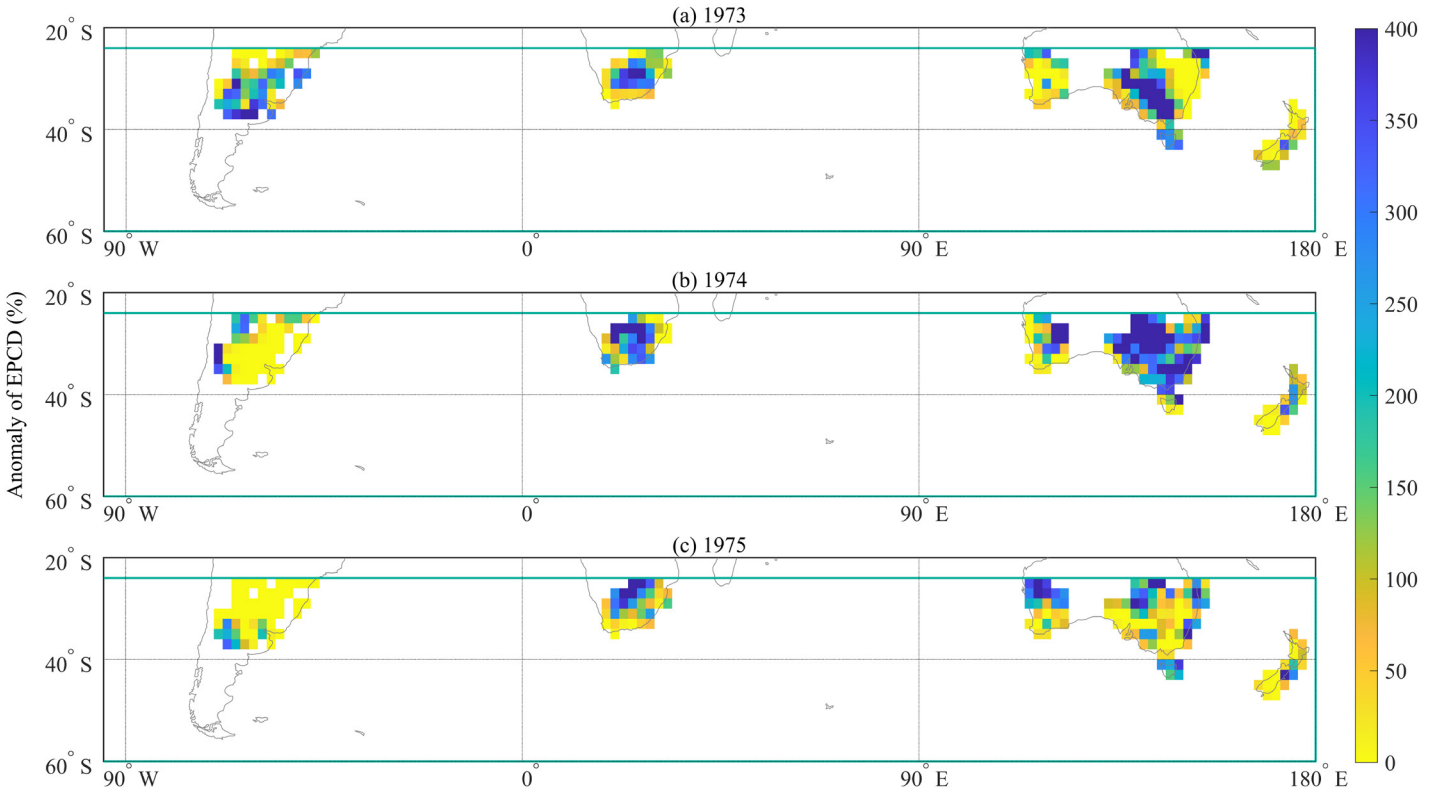

Fig. ES10. Local- and regional-mean changes in the frequency of extreme precipitation on consecutive days for historical simulations of all 30 models using the spatial coverage mask of the observations. (a) Local changes (%) between 1961–85 and 1986–2010 for the historical simulations identified from the ensemble mean of the 30 CMIP5 simulations. (b) The corresponding regional-average changes (%) between both periods. The difference is a relative frequency change (see "Materials and methods" section in the main text). The asterisk in (b) indicates a "robust change" across all models (see "Materials and methods" section in the main text). Error bars in (b) represent plus and minus one ensemble standard deviation. The colored boxes or outlines in (a) define the regions for calculating the regional averages as presented by bars of the corresponding colors in (b).

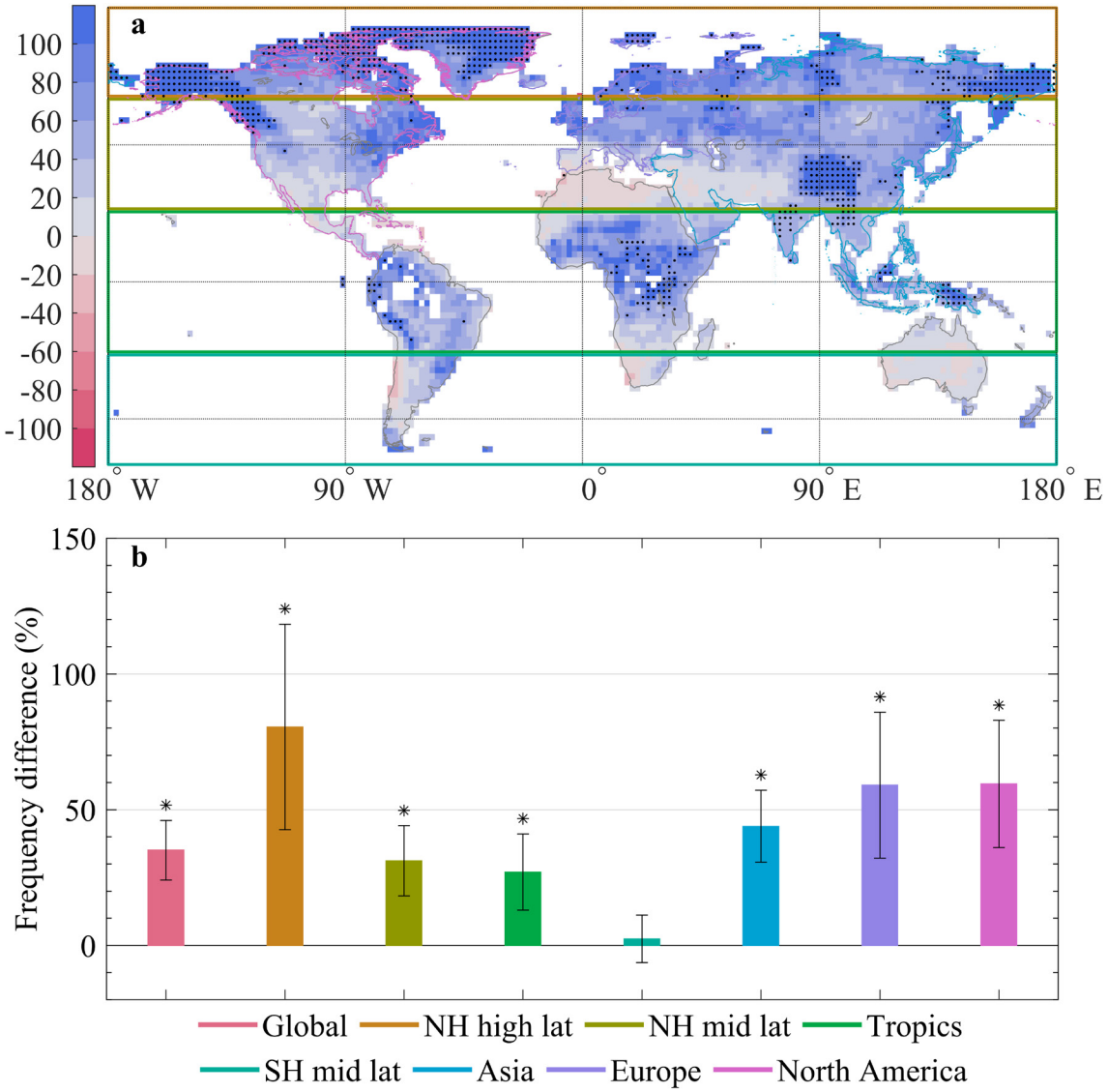

Fig. ES11. Local- and regional-mean changes in the frequency of extreme precipitation on consecutive days for RCP4.5 scenario simulations of all 30 models. (a) Local changes (%) between 1961–2010 (from the historical simulations) and 2071–100 for RCP4.5 scenario identified from the ensemble mean of the 30 CMIP5 simulations. (b) The corresponding regional-average changes (%) between both periods. The difference is a relative frequency change (see "Materials and methods" section in the main text). The stippling in (a) and the asterisks in (b) indicate a "robust change" across all models (see "Materials and methods" section in the main text). Error bars in (b) represent plus and minus one ensemble standard deviation. The colored boxes or outlines in (a) define the regions for calculating the regional averages as presented by bars of the corresponding colors in (b).

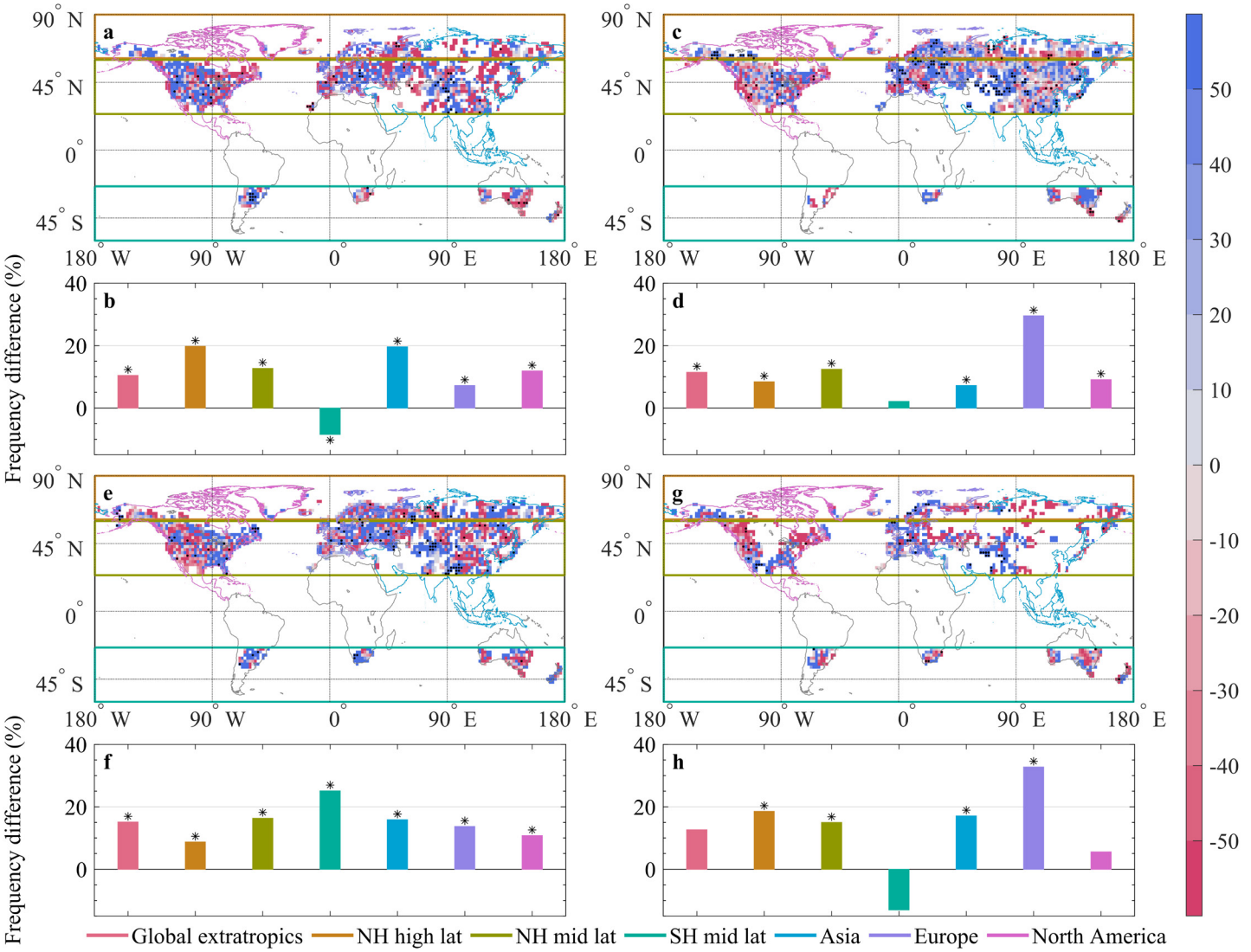

Fig. ES12. Changes in seasonal frequency of extreme precipitation on consecutive days between 1961–85 and 1986–2010 identified from observations. (a),(b) Local and regional changes (%) in mean frequency between 1961–85 and 1986–2010 for March–May (MAM). (c),(d) Local and regional changes (%) for June–August (JJA). (e),(f) Local and regional changes (%) for September–November (SON). (g),(h) Local and regional changes (%) for December–February (DJF). Colored regions and significance test of the changes are as in Fig. ES8.

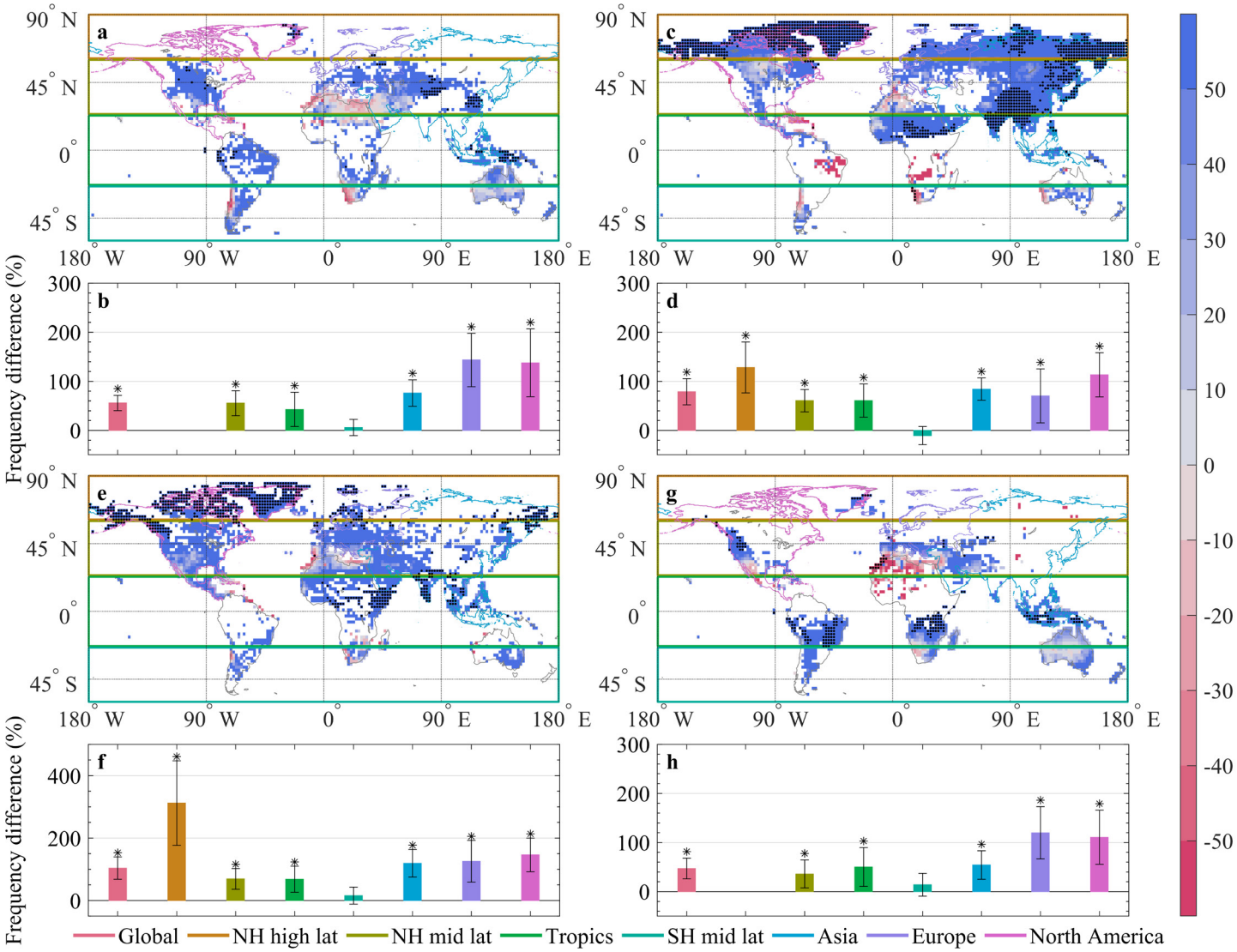

Fig. ES13. Changes in seasonal frequency of extreme precipitation on consecutive days between 1961–2010 and 2071–100 identified from historical + RCP8.5 scenario simulations. (a),(b) Local and regional changes (%) in mean frequency between 1961–2010 and 2071–100 for MAM. (c),(d) Local and regional changes (%) for JJA. (e),(f) Local and regional changes (%) for SON. (g),(h) Local and regional changes (%) for DJF. Blank grids indicate there is no extreme precipitation on consecutive days during 1961–2010. Regional changes are not shown when the available grid cells are few. Colored regions and significance test of the changes are as in Fig. ES11.

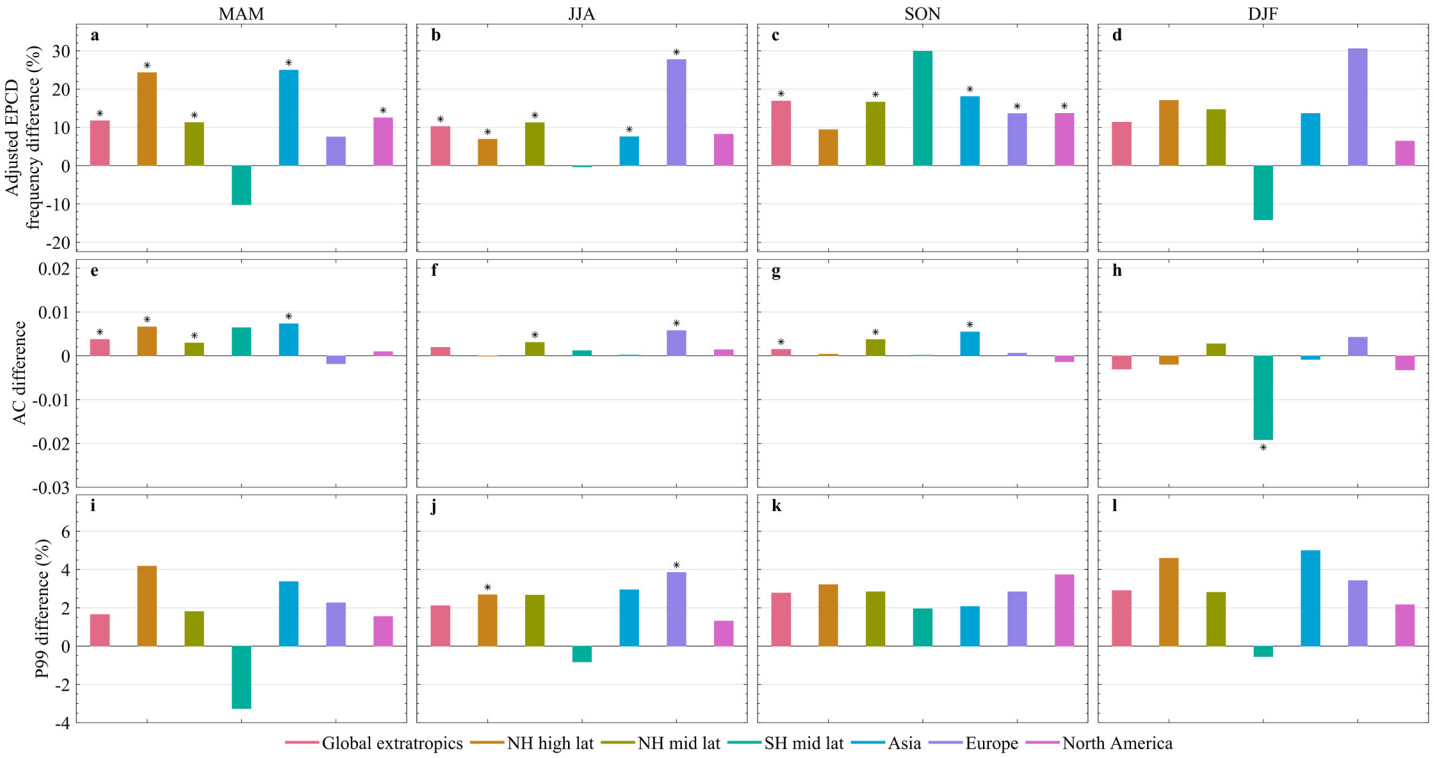

Fig. ES14. Regional changes in seasonal adjusted EPCD frequency, autocorrelation, and precipitation intensity between 1961–85 and 1986–2010 for observations. (a)–(d) Changes (%) in the adjusted EPCD frequency after removing the effects of possible intensity changes (see "Materials and methods" section in the main text) for MAM, JJA, SON, and DJF, respectively. (e)–(h) Changes in autocorrelation in the daily extreme precipitation time series. (i)–(l) Changes (%) in daily intensity of precipitation for the 99th percentile of all-day precipitation. Colored regions and significance test of the changes are as in Fig. ES8.

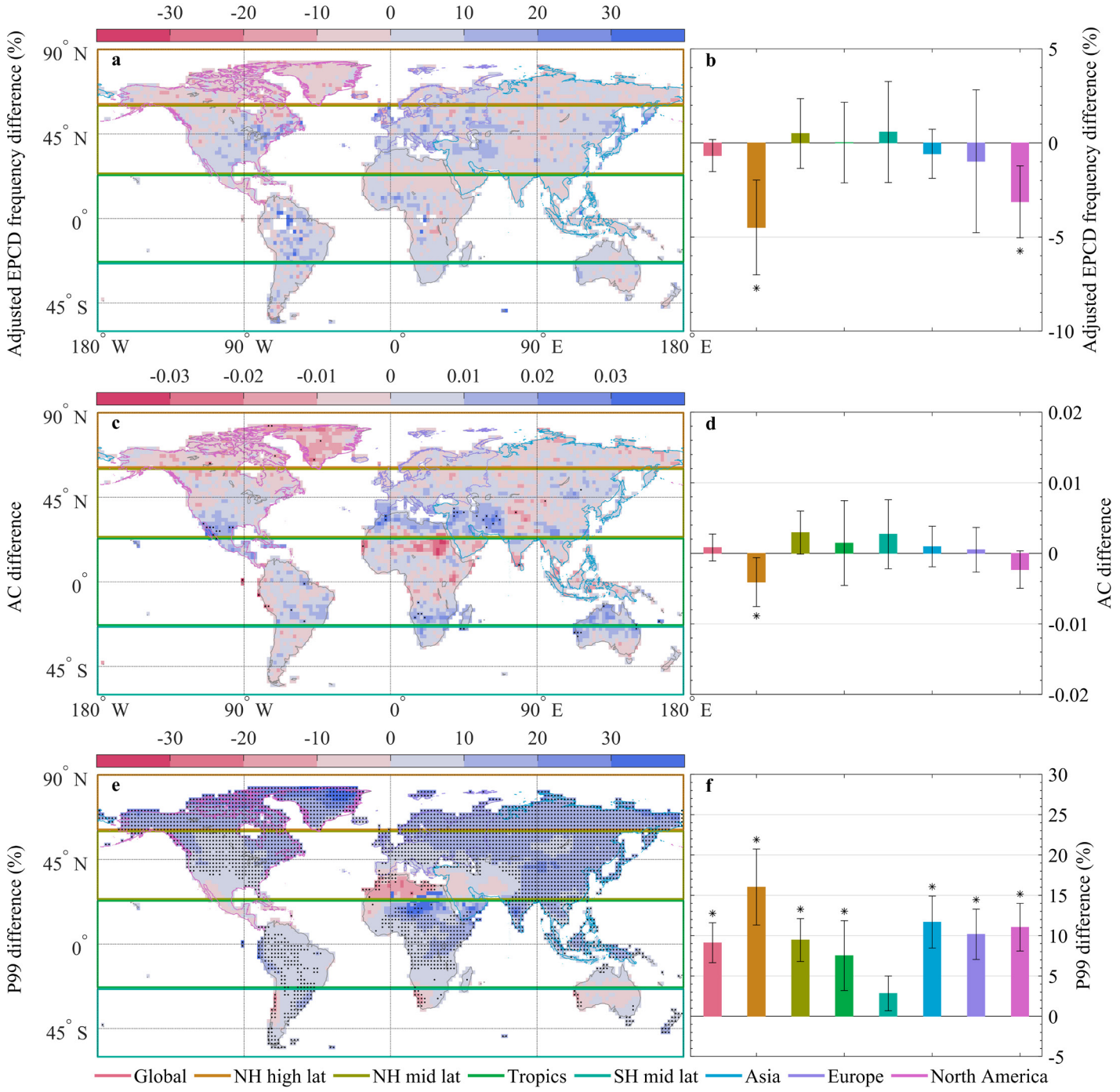

Fig. ES15. Local and regional changes in adjusted frequency of extreme precipitation on consecutive days, autocorrelation, and precipitation intensity for RCP4.5 scenario simulations. (a),(b) EPCD frequency changes (%) after removing the effects of possible intensity changes (by definition in the "Materials and methods" section in the main text). (c),(d) Changes in autocorrelation in the daily extreme precipitation time series. (e),(f) Changes (%) in daily intensity of precipitation for the 99th percentile of all-day precipitation. Changes are calculated between 1961–2010 (from the historical simulations) and 2071–2100 for RCP4.5 scenario identified from the ensemble mean of the 30 CMIP5 simulations. The significance of changes is estimated by the Wilcoxon rank sum test. The colored boxes or outlines in (a), (c), and (e) define the regions for calculating the regional averages as presented by bars of the corresponding colors in (b), (d), and (f).

Use of model data

Tables ES1 and ES2 provide additional information on the climate models.

Table ES1. Information on the 30 global climate models.

Model name	Center, country/region	Resolution (lat × lon)
ACCESS 1.0	CSIRO-BOM, Australia	1.24° × 1.87°
ACCESS 1.3	CSIRO-BOM, Australia	1.24° × 1.87°
BCC_CSM1.1	BCC, China	2.81° × 2.81°
BCC_CSM1.1(m)	BCC, China	1.12° × 1.12°
BNU-ESM	BNU, China	2.81° × 2.81°
CanESM2	CCCma, Canada	0.93° × 1.25°
CCSM4	NCAR, United States	0.93° × 1.25°
CESM1-BGC	NSF–DOE–NCAR, United States	0.93° × 1.25°
CESM1-CAM5	NSF–DOE–NCAR, United States	3.75° × 3.75°
CMCC-CM	CMCC, Europe	2.81° × 2.81°
CMCC-CMS	CMCC, Europe	1.40° × 1.40°
CNRM-CM5	CNRM, France	2.81° × 2.81°
FGOALS-g2	LASG-IAP, China	3.00° × 2.81°
GFDL-CM3	NOAA GFDL, United States	2.00° × 2.50°
GFDL-ESM2G	NOAA GFDL, United States	2.00° × 2.50°
GFDL-ESM2M	NOAA GFDL, United States	2.00° × 2.50°
HadGEM2-AO	MOHC, United Kingdom	1.24° × 1.87°
HadGEM2-CC	MOHC, United Kingdom	1.24° × 1.87°
HadGEM2-ES	MOHC, United Kingdom	1.24° × 1.87°
inmcm4	INM, Russia	1.25° × 2.50°
IPSL-CM5A-LR	IPSL, France	1.87° × 3.75°
IPSL-CM5A-MR	IPSL, France	1.25° × 2.50°
IPSL-CM5B-LR	IPSL, France	1.87° × 3.75°
MIROC5	MIROC, Japan	1.40° × 1.40°
MIROC-ESM	MIROC, Japan	2.81° × 2.81°
MIROC-ESM-CHEM	MIROC, Japan	2.81° × 2.81°
MPI-ESM-LR	MPI-M, Germany	1.87° × 1.87°
MPI-ESM-MR	MPI-M, Germany	1.87° × 1.87°
MRI-CGCM3	MRI, Japan	1.12° × 1.12°
NorESM1-M	NCC, Norway	1.87° × 2.50°

Table ES2. Information on the 22 regional climate models.

Region	Model name	Center, country/region	Resolution (lat × lon)
Europe	CNRM-CM5-CLMcom-CCLM4-8-17	CLMcom	0.11° × 0.11°
	CNRM-CM5-RMIB-UGent-ALARO-0	RMIB-UGent, Belgium	0.11° × 0.11°
	ICHEC-EC-EARTH-DMI-HIRHAM5	DMI, Denmark	0.11° × 0.11°
	ICHEC-EC-EARTH-KNMI-RACMO22E	KNMI, the Netherlands	0.11° × 0.11°
	IPSL-CM5A-MR-WRF381P	IPSL, France	0.11° × 0.11°
	IPSL-CM5A-MR-RACMO22E	KNMI, the Netherlands	0.11° × 0.11°
	HadGEM2-ES-CCLM4-8-17	CLMcom	0.11° × 0.11°
	HadGEM2-ES-WRF381P	IPSL, France	0.11° × 0.11°
	MPI-ESM-LR-CLMcom-CCLM4-8-17	CLMcom	0.11° × 0.11°
	MPI-ESM-LR-KNMI-RACMO22E	KNMI, the Netherlands	0.11° × 0.11°
	MPI-ESM-LR-MPI-CSC-REMO2009	MPI-CSC, Germany	0.11° × 0.11°
	NCC-NorESM1-M-IPSL-WRF381P	IPSL, France	0.11° × 0.11°
	NCC-NorESM1-M-KNMI-RACMO22E	KNMI, the Netherlands	0.11° × 0.11°
North America	CanESM2-CanRCM4	CCCma, Canada	0.22° × 0.22°
	CanESM2-CRCM5-OUR	OURANOS	0.22° × 0.22°
	CanESM2-CRCM5-UQAM	UQAM, Canada	0.22° × 0.22°
	GEMatm-Can-CRCM5-UQAM	UQAM, Canada	0.22° × 0.22°
	GFDL-ESM2M-CRCM5-OUR	OURANOS	0.22° × 0.22°
	GFDL-ESM2M-RegCM4	NCAR, United States	0.22° × 0.22°
	HadGEM2-ES-RegCM4	NCAR, United States	0.22° × 0.22°
	HadGEM2-ES-WRF	NCAR, United States	0.22° × 0.22°
	MPI-ESM-LR-CRCM5-OUR	OURANOS	0.22° × 0.22°